JPhys Materials

PAPER

Deciphering the origin of nonlocal resistance in multiterminal graphene on hexagonal-boron-nitride with *ab initio* quantum transport: Fermi surface edge currents rather than Fermi sea topological valley currents

J M Marmolejo-Tejada[1,2,9] , J H García[3] , M D Petrović[4], P-H Chang[5], X-L Sheng[1,6], A Cresti[7] , P Plecháč[4], S Roche[3,8] and B K Nikolić[1]

1   Department of Physics and Astronomy, University of Delaware, Newark, DE 19716, United States of America
2   School of Electrical and Electronics Engineering, Universidad del Valle, Cali, AA 25360, Colombia
3   Catalan Institute of Nanoscience and Nanotechnology (ICN2), CSIC and The Barcelona Institute of Science and Technology, Campus UAB, Bellaterra, E-08193 Barcelona, Spain
4   Department of Mathematical Sciences, University of Delaware, Newark, DE 19716, United States of America
5   Department of Physics and Astronomy, University of Nebraska Lincoln, Lincoln, NE 68588, United States of America
6   Department of Applied Physics, Beihang University, Beijing 100191, People's Republic of China
7   Univ. Grenoble Alpes, CNRS, Grenoble INP, IMEP-LaHC, F-38000 Grenoble, France
8   ICREA—Institucio Catalana de Recerca i Estudis Avançats, E-08010 Barcelona, Spain
9   Electronics Engineering and Computer Science Division, Pontificia Universidad Javeriana, Cali, Colombia
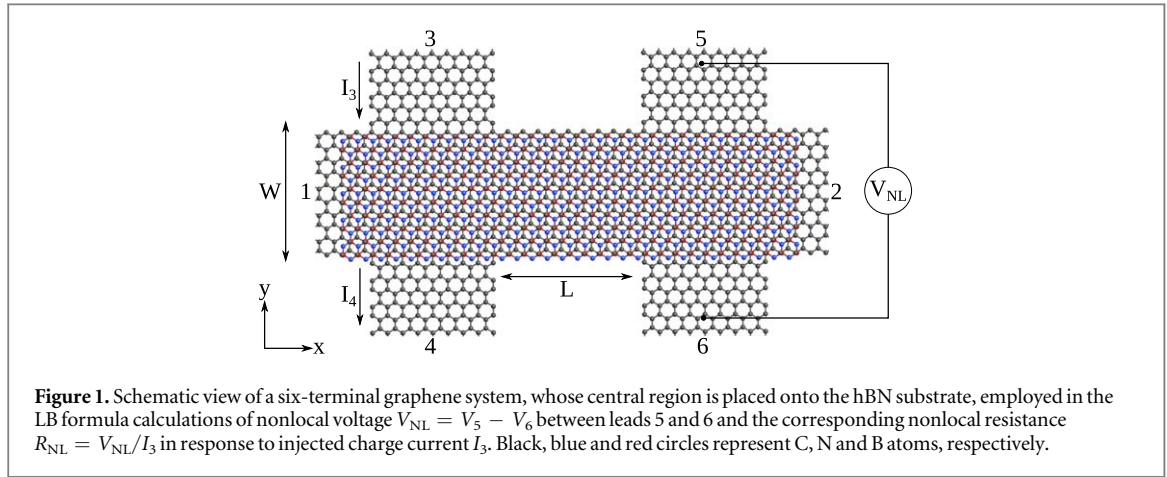
E-mail: bnikolic@udel.edu

Abstract

The recent observation (Gorbachev *et al* 2014 *Science* **346** 448) of nonlocal resistance R_{NL} near the Dirac point (DP) of multiterminal graphene on aligned hexagonal-boron nitride (G/hBN) has been interpreted as the consequence of topological valley Hall currents carried by the Fermi sea states just beneath the bulk gap E_g induced by inversion symmetry breaking. However, the corresponding valley Hall conductivity σ_{xy}^v, quantized inside E_g, is not directly measurable. Conversely, the Landauer–Büttiker formula, as a numerically exact approach to observable nonlocal transport quantities, yields $R_{NL} \equiv 0$ for the same simplistic Hamiltonian of gapped graphene that generates $\sigma_{xy}^v \neq 0$ via the Kubo formula. We combine *ab initio* with quantum transport calculations to demonstrate that G/hBN wires with zigzag edges host dispersive edge states near the DP that are absent in theories based on the simplistic Hamiltonian. Although such edge states exist also in isolated zigzag graphene wires, aligned hBN is required to modify their energy–momentum dispersion and generate $R_{NL} \neq 0$ near the DP. The Fermi surface-determined edge currents carrying the nonlocal signal persist also in the presence of edge disorder and over long distances. Concurrently, they resolve the long-standing puzzle of why the highly insulating state of G/hBN is rarely observed. *Thus, we conclude that the observed R_{NL} is unrelated to Fermi sea topological valley currents conjectured for gapped Dirac spectra.*

The recent measurements [1] of a sharply peaked nonlocal resistance R_{NL} in a narrow energy range near the Dirac point (DP) of multiterminal graphene on hexagonal-boron nitride (G/hBN) heterostructures have been interpreted as the manifestation of the valley Hall effect (VHE) [2–5]. In this interpretation, injecting charge current I_3 between leads 3 and 4 of the device illustrated in figure 1 generates a VH current in the first crossbar flowing from lead 1 to lead 2, which traverses the channel of length L ($\simeq 4$ μm in the experiments [1]), and is finally converted into a nonlocal voltage V_{NL} between leads 5 and 6 by the inverse VHE in the second crossbar. The corresponding nonlocal resistance $R_{NL} = V_{NL}/I_3$ has been observed previously also near the DP in multiterminal graphene due to an external magnetic field inducing edge states in the quantum Hall regime or the

Figure 1. Schematic view of a six-terminal graphene system, whose central region is placed onto the hBN substrate, employed in the LB formula calculations of nonlocal voltage $V_{NL} = V_5 - V_6$ between leads 5 and 6 and the corresponding nonlocal resistance $R_{NL} = V_{NL}/I_3$ in response to injected charge current I_3. Black, blue and red circles represent C, N and B atoms, respectively.

Zeeman spin Hall effect at higher temperatures [6–10], as well as due to the spin Hall effect [10–12]. However, none of these mechanisms is operational in the experiment of [1].

Instead, the physics of graphene on hBN with their crystallographic axes *aligned* is expected to be governed by the broken spatial inversion symmetry due to different potentials on two triangular sublattices of carbon atoms induced by the hBN substrate. This opens a gap E_g at the DP of two valleys K and K' in the band structure of an infinite two-dimensional sheet of graphene, where *ab initio* calculations have estimated $E_g \simeq 58$ meV [13]. In addition, the finite Berry curvature [14] of opposite sign at the two valleys was predicted to generate valley-dependent transverse conductivities, $\sigma_{xy}^K = e^2/h$ and $\sigma_{xy}^{K'} = -e^2/h$ [2–4]. The VH current is characterized by the transverse VH conductivity, $\sigma_{xy}^v = \sigma_{xy}^K - \sigma_{xy}^{K'} = 2e^2/h$, and zero transverse charge conductivity, $\sigma_{xy} = \sigma_{xy}^K + \sigma_{xy}^{K'} \equiv 0$, within the gap [3, 4, 15]. Such charge-neutral valley currents, denoted also as 'topological' [1–4] due to the involvement of the Berry curvature hot spots in reciprocal space, are not conserved but are expected to be long-ranged when the intervalley scattering is weak [15].

However, σ_{xy}^v is *not directly observable*. An attempt to connect σ_{xy}^v to observable nonlocal resistance is made [1, 4, 5]

$$R_{NL} \propto (\sigma_{xy}^v)^2 \rho_{xx}^3 e^{-L/\ell_v}, \tag{1}$$

using semiclassical transport theory [16], which assumes diffusive transport with ℓ_v as the valley diffusion length [5]. However, semiclassical transport theory is not applicable [17, 18] to electronic transport near the DP. In the case of G/hBN, this is further emphasized [19] by the presence of the gap forcing electrons to tunnel through the system, which is a phenomenon with no classical analog.

The Landauer–Büttiker (LB) formalism [20–22], which offers quantum transport framework to compute V_{NL} and R_{NL} directly and has been used for decades to model nonlocal transport measurements [23, 24], yields $R_{NL} \equiv 0$ near the DP in figure 2(c) in multiterminal geometries whose channel length is larger than its width ($L/W \simeq 4$ in the experiments of [1]). Note that in geometries with $L < W$, we (as well as [19]) get $R_{NL} \neq 0$ in figure 2(c). Nevertheless, this is trivially explained by transport through evanescent wave-functions able to propagate from the first to the second crossbar through the gap in such geometries [12, 19].

The *numerically exact* result in figure 2(c), for a G/hBN system described by the same simplistic Hamiltonian employed [1–4, 15] to obtain $\sigma_{xy}^v \neq 0$, is clearly incompatible with the interpretation of $R_{NL} \neq 0$ based on the picture of topological valley currents carried by the Fermi sea states just beneath the gap [3]. Such currents are conjectured to be persistent and circulating in equilibrium [3], but they become mediative VH currents connecting the two crossbars in figure 1 under the application of a bias voltage. Thus, this concept circumvents the absence of electronic states around the DP, but at a very high price—it demands *a major overhaul of the LB theory* [21] in which the absence of states within the gap is a fundamental reason for $R_{NL} \equiv 0$ in figure 2(c).

Another *long-standing puzzle* is the metallic-like ordinary longitudinal resistivity, $\rho_{xx} \sim 10$ kΩ, commonly measured experimentally [1, 25] for the G/hBN channel between the two crossbars despite the expected finite gap in its bulk. This suggests the presence of additional conduction pathways, such as edge currents observed very recently [26, 27], which shunt the highly insulating state at low temperatures. However, previous studies have concluded that edge states are either absent [3] or, when they are present due to zigzag [28, 29] or chiral [30, 31] arrangement of edge carbon atoms, they become gapped near the DP and dispersionless away from it so they *cannot* carry any current [32]. The latter conclusion is reproduced in figure A1(f) in appendix A where we compute the band structure of a G/hBN wire with zigzag edges using the same simplistic Hamiltonian employed in prior theoretical studies [1–4, 15, 19, 32].
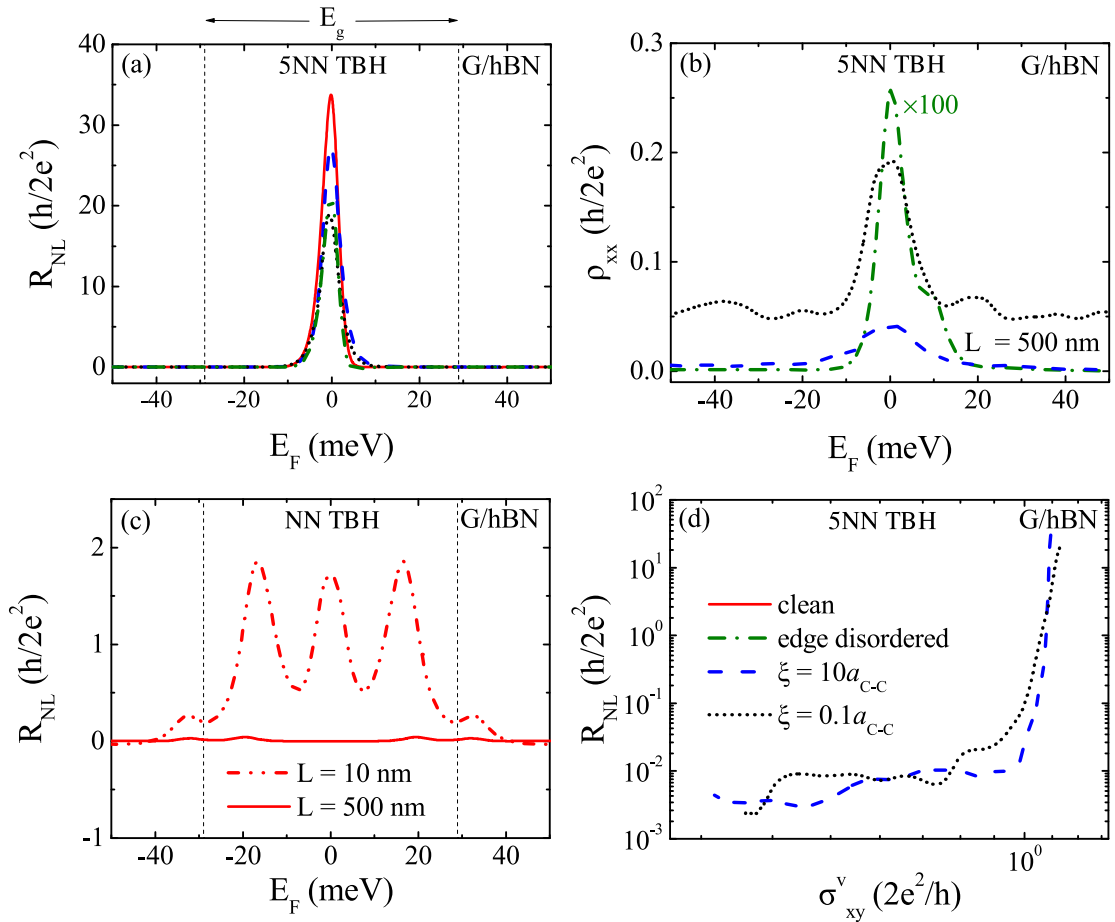
Figure 2. (a), (c), (d) Nonlocal resistance R_{NL} and (b) longitudinal resistivity ρ_{xx} for the device in figure 1 whose channel has width $W = 50\,nm$ and length $L = 500\,nm$, as well as $L = 10\,nm$ in panel (c). We use *ab initio* 5NN TBH to describe the G/hBN channel with zigzag edges in panels (a), (b), (d); while NN TBH in equation (12), employed in previous theoretical studies [1–4, 15, 19, 32], is used in panel (c). The disorder is introduced either by removing carbon atoms along the edges of the channel (figure C1(b) in appendix C), or by adding impurities into its bulk with 30% concentration and long-range ($\xi = 10a_{C-C}$, where a_{C-C} is carbon–carbon bond length, and strength $U_p = 1.275\,eV$ in the model explained in appendix D) or short-range ($\xi = 0.1a_{C-C}$ and effective strength $0.005 \times U_p$) potential. The disorder averaging is performed over 10 samples. The temperature is set at $T = 20\,K$, as in the experiment of [1].

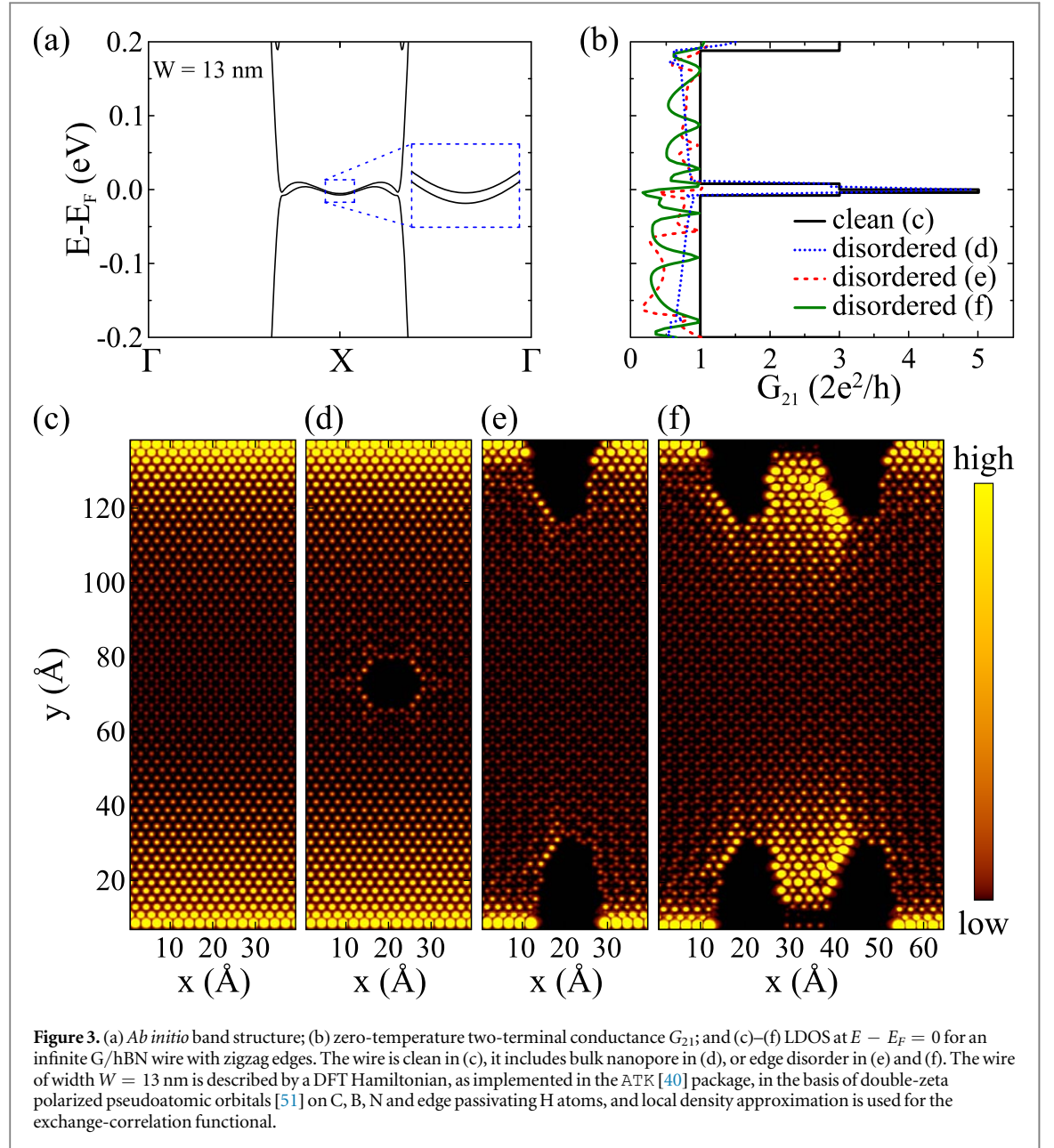In this work, we demonstrate how to resolve *both puzzles*:

- $R_{NL} \equiv 0$ (figure 2(c)) obtained for multiterminal G/hBN whose bulk counterpart exhibits $\sigma^v_{xy} \neq 0$ (figure 4(a)),

- metallic-like ρ_{xx} usually measured experimentally [1, 25] despite the presumed gap opening around the DP,

using *ab initio* quantum transport where we perform density functional theory (DFT) calculations combined with both the multiterminal LB formula (figures 2, 3 and 5) and the Kubo formula (figure 4).

These puzzles turn out to be an artifact of the simplistic Hamiltonian [1–4, 15, 19, 32], which inadequately describes G/hBN wires. For example, in contrast to previously obtained [32] gapped band structure for all types of G/hBN wires, the *ab initio* band structure (figure 3(a)) of G/hBN wires with zigzag edges has no gap. The *ab initio* Hamiltonian combined with the LB formula yields R_{NL} (figure 2(a)) and ρ_{xx} (figure 2(b)) whose features closely match those measured in [1]:

- the ρ_{xx} peak is wider than the R_{NL} peak,

- the magnitude of the R_{NL} peak decays exponentially with increasing L (figure 5(b)),

- aligned hBN is *necessary* to obtain $R_{NL} \neq 0$ in figure 2(a)—an isolated zigzag graphene wire also has edge states (figure B1(a)–(f) in appendix B), but its band structure leads to $R_{NL} \equiv 0$ (figure B2 in appendix B).

Since the resolution of the two puzzles relies on an accurate Hamiltonian for G/hBN wires, as well as its combination with a proper quantum theory of observable transport quantities, we first summarize

Figure 3. (a) *Ab initio* band structure; (b) zero-temperature two-terminal conductance G_{21}; and (c)–(f) LDOS at $E - E_F = 0$ for an infinite G/hBN wire with zigzag edges. The wire is clean in (c), it includes bulk nanopore in (d), or edge disorder in (e) and (f). The wire of width $W = 13$ nm is described by a DFT Hamiltonian, as implemented in the ATK [40] package, in the basis of double-zeta polarized pseudoatomic orbitals [51] on C, B, N and edge passivating H atoms, and local density approximation is used for the exchange-correlation functional.

inconsistencies arising in previous theoretical analyses. The seminal arguments [2] for the VHE are based on the semiclassical transport theory describing the motion of a narrow wave-packet constructed by superposing [2, 33] eigenstates of gapped Dirac Hamiltonian $\hat{H}_D$ with dispersion $\epsilon_{\mathbf{k}}$. This assumes that each valley of G/hBN can be described by
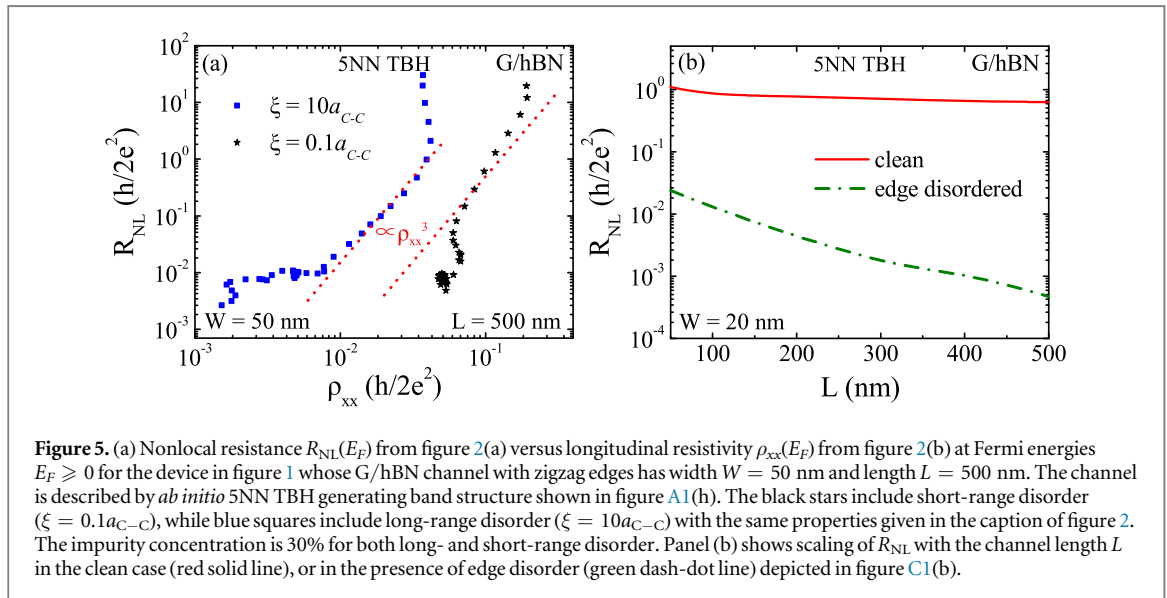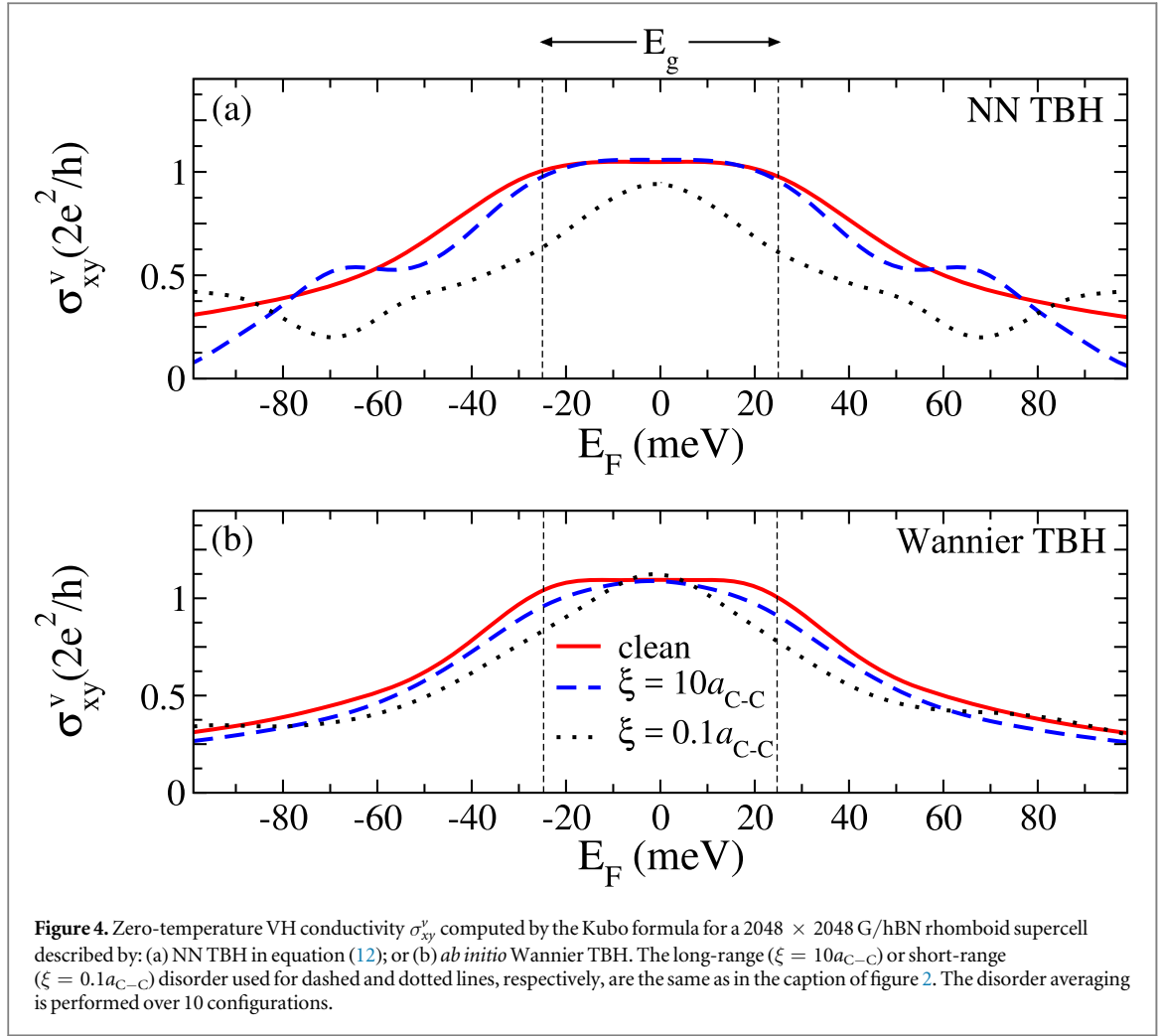
$$\hat{H}_D = \hbar v_F (\hat{\boldsymbol{\sigma}} \cdot \hat{\mathbf{k}}) + \Delta \hat{\sigma}_z, \tag{2}$$

where v_F is the Fermi velocity, $\hat{\boldsymbol{\sigma}} = (\hat{\sigma}_x, \hat{\sigma}_y)$ is the vector of the Pauli matrices corresponding to the sublattice degree of freedom and $\hbar \hat{\mathbf{k}}$ is the momentum operator. The wave-packet velocity

$$\mathbf{v}_{\mathbf{k}} = \frac{1}{\hbar} \frac{\partial \epsilon_{\mathbf{k}}}{\partial \mathbf{k}} + \frac{d\mathbf{k}}{dt} \times \boldsymbol{\Omega}_{\mathbf{k}}, \tag{3}$$

acquires an anomalous (second) term [14] due to the Berry curvature $\Omega_{\mathbf{k}}$ hot spot near the apex of the valley described by $\hat{H}_D$. Since $\boldsymbol{\Omega}_{\mathbf{k}}$ in valley K has opposite direction to that in valley K', electrons belonging to two valleys will be separated [33] in the opposite transverse directions in the presence of an applied electric field $\mathbf{E}$, which is required to accelerate electrons according to $\hbar d\mathbf{k}/dt = e\mathbf{E}$. This gives rise [2] to

$$\sigma_{xy}^{K,K'} = \frac{e^2}{\pi h} \int d^2 \mathbf{k} \, f(\varepsilon_{\mathbf{k}}) \Omega_{\mathbf{k}}, \tag{4}$$

Figure 4. Zero-temperature VH conductivity σ_{xy}^v computed by the Kubo formula for a 2048×2048 G/hBN rhomboid supercell described by: (a) NN TBH in equation (12); or (b) *ab initio* Wannier TBH. The long-range ($\xi = 10a_{C-C}$) or short-range ($\xi = 0.1a_{C-C}$) disorder used for dashed and dotted lines, respectively, are the same as in the caption of figure 2. The disorder averaging is performed over 10 configurations.

Figure 5. (a) Nonlocal resistance $R_{NL}(E_F)$ from figure 2(a) versus longitudinal resistivity $\rho_{xx}(E_F)$ from figure 2(b) at Fermi energies $E_F \geqslant 0$ for the device in figure 1 whose G/hBN channel with zigzag edges has width $W = 50$ nm and length $L = 500$ nm. The channel is described by *ab initio* 5NN TBH generating band structure shown in figure A1(h). The black stars include short-range disorder ($\xi = 0.1a_{C-C}$), while blue squares include long-range disorder ($\xi = 10a_{C-C}$) with the same properties given in the caption of figure 2. The impurity concentration is 30% for both long- and short-range disorder. Panel (b) shows scaling of R_{NL} with the channel length L in the clean case (red solid line), or in the presence of edge disorder (green dash-dot line) depicted in figure C1(b).

where $f(\varepsilon_\mathbf{k})$ is the Fermi function forcing the integration over the whole Fermi sea, i.e. from the bottom of the band to the Fermi level E_F.

However, it has already been pointed out in [19] that nonzero **E** *cannot* appear in the linear-response limit of the multiterminal LB formula [20–22]. The experiments measuring R_{NL} are carefully kept [1] in the linear-response regime in order to avoid heating of the device and the ensuing thermoelectric effects that can add large spurious contributions to R_{NL} [7]. The multiterminal LB formula

$$I_p = \sum_q G_{pq}(V_p - V_q), \tag{5}$$

relates the total charge current I_p in lead p to voltages V_q in all other leads via the conductance coefficients

$$G_{pq} = \frac{2e^2}{h} \int dE \left(-\frac{\partial f}{\partial E} \right) T_{pq}(E), \tag{6}$$

where the negative derivative of the Fermi function confines the integration to a shell of states of width $\sim k_B T$ around E_F [21]. The transmission functions $T_{pq}(E)$ do not include any effect of **E** [20–22]. We use the multiterminal LB formula implemented in KWANT package [22, 34] to compute

$$V_{\mathrm{NL}} = V_5 - V_6, \tag{7}$$

and

$$R_{\mathrm{NL}} = \frac{V_{\mathrm{NL}}}{I_3}, \tag{8}$$

in response to an injected charge current $I_3 = -I_4$ [12] while keeping $I_p \equiv 0$ in the other four leads. A similar procedure allows us to compute the longitudinal resistivity

$$\rho_{xx} = R_{\mathrm{4T}} \frac{W}{L}, \tag{9}$$

from the four-terminal resistance

$$R_{\mathrm{4T}} = \frac{V_3 - V_5}{I_1}, \tag{10}$$

obtained by injecting the current $I_1 = -I_2$ into the device of figure 1 and by imposing voltage probe conditions, $I_p \equiv 0$, in leads $p = 3$–6.

The semiclassical arguments for the origin of σ_{xy}^v can be replaced by quantum transport theory based on the Kubo formula [15, 35], which requires to first obtain [36, 37] the velocity operator $\hat{\mathbf{v}}$. The physical consequences of the equation of motion for $\hat{\mathbf{v}} = v_F \hat{\boldsymbol{\sigma}}$ defined by $\hat{H}_D$ [15]

$$\frac{d\mathbf{v}}{dt} = \frac{1}{i\hbar}[\hat{\mathbf{v}}, \hat{H}_D] = 2v_F^2(\hat{\mathbf{k}} \times \hat{\boldsymbol{\sigma}}) - \frac{E_g}{\hbar}\hat{\mathbf{v}} \times \mathbf{e}_z, \tag{11}$$

are extracted by finding its expectation value in a suitably prepared wave-packet [33, 38] injected with given initial velocity into G/hBN, where it can propagate even in the absence of any external electric field [38]. The first term of $d\mathbf{v}/dt$ causes *Zitterbewegung* motion of the center of the wave-packet, while the second one acts on it like a Lorentz force due to an effective magnetic field in the direction of the unit vector $\mathbf{e}_z$ perpendicular to the graphene plane. For electrons from the K' valley, $\hat{v}_y = -v_F \hat{\sigma}_y$, leading to opposite direction of this force.

The gapped Dirac Hamiltonian $\hat{H}_D$ is a long wavelength limit of a more general tight-binding Hamiltonian (TBH). This latter accounts for both valleys and can, therefore, be used to capture intervalley scattering effects. The TBH, which is preferred for numerical calculations using the LB [19] or the Kubo formula (as well as for simulations of wave-packet dynamics [33]), is defined on a honeycomb lattice hosting a single p_z-orbital *per* site

$$\hat{H}_{\mathrm{TB}} = \sum_i \varepsilon_i \hat{c}_i^\dagger \hat{c}_i - t_1 \sum_{\langle ij \rangle} \hat{c}_i^\dagger \hat{c}_j. \tag{12}$$

Here, $\hat{c}_i^\dagger$ ($\hat{c}_i$) creates (annihilates) an electron at site i; the hopping energy $t_1 = 2.7$ eV is nonzero between nearest-neighbor (NN) carbon atoms; and the on-site energy $\varepsilon_i = \pm\Delta$, responsible for the gap $E_g = 2\Delta$, is positive on one atom of the graphene unit cell and negative on the other one to take into account the staggered potential induced by the hBN substrate (while neglecting any reorganization of chemical bonding or change in the atomic order of graphene and hBN layers). We use $\Delta = 29$ meV [13] to compute R_{NL} in figure 2(c) for G/hBN channel with zigzag edges, as well as to compute its band structure (figure A1(f) in appendix A) exhibiting gapped flat bands [32].

Figure 4(a) shows σ_{xy}^v, computed using the Kubo formula [35, 37] combined with a valley-projection scheme [10, 39], for a rhomboid supercell of G/hBN with periodic boundary conditions described by $\hat{H}_{\mathrm{TB}}$ in equation (12). The supercell is either clean or it contains long- or short-range disorder (delineated in appendix D) as additional terms in the on-site energy ε_i. In the clean limit, we confirm [15] that $\sigma_{xy}^v = 2e^2/h$ is quantized inside the gap (figure 4(a)), as well as that the Fermi sea states just beneath the gap provide the main contribution to it [3]. For long-range disorder that does not mix valleys, σ_{xy}^v remains close to the clean limit, but within a smaller energy range than E_g (figure 4(a)) due to disorder-induced broadening of the states [15]. High concentration of valley mixing short-range disorder slightly reduces σ_{xy}^v (figure 4(a)).

In order to replace $\hat{H}_{\mathrm{TB}}$ with a more accurate Hamiltonian, we proceed by computing the *ab initio* band structure of G/hBN wires using local-orbital pseudopotential DFT, as implemented in ATK [40] and OpenMX

[41] packages, whose Kohn–Sham (KS) Hamiltonian can be also easily combined with the LB formula [42]. We assume stacking where one C atom is over a B atom and the other C atom in the unit cell is centered above the hBN hexagon, as the energetically most stable configuration found in DFT calculations [13]. The DFT Hamiltonian for a wire—composed of C, B and N atoms, as well as H atoms passivating dangling bonds along the zigzag edges—produces the gapless band structure in figure 3(a) and the corresponding zero-temperature two-terminal conductance $G_{21} = 5 \times 2e^2/h$ (figure 3(b)) near the DP (at $E - E_F = 0$). This value is insensitive to the presence of a nanopore within the bulk (figure 3(d)), signifying edge transport, but it is reduced to $G_{21} \lesssim 2e^2/h$ in the presence of edge vacancies (figure 3(e)) or quantum interferences generated by edge vacancies in series (figure 3(f)) due to lack of topological protection against backscattering [32, 43]. The valley-polarized states [44] above and below the DP are bulk states since G_{21} is reduced at those energies by the presence of the bulk nanopore (figure 3(d)). The edge states are visualized by plotting the local density of states (LDOS) in figures 3(c)–(f), which is peaked near the edges but it remains nonzero in the bulk [31]. This can be contrasted with topologically protected edge states in quantum (ordinary [10], spin [45, 46] and anomalous [47]) Hall insulators, where LDOS in the bulk vanishes. The corresponding local current distributions (figure C1 in appendix C) shows that edge currents can survive edge disorder breaking G/hBN wire into short zigzag-edge segments, as suggested also by experiments [26]. The G/hBN wires with pristine armchair edges do not exhibit any edge states (figures B1(g)–(l) in appendix B), which, therefore, leads to $R_{NL} \equiv 0$ in multiterminal geometries with $L > W$.

It is worth mentioning that even in systems with nonzero topological invariants in the bulk band structure, such as the Chern number $\mathcal{C}$ in quantum Hall and quantum anomalous Hall insulators, which counts the number of metallic edge states [32] (note that $\mathcal{C} \equiv 0$ in the case of G/hBN [32]), zigzag edges of the honeycomb lattice play a special role due to their ability to modify the energy–momentum dispersion and the corresponding conductance carried by edge states [47]. They also shrink the spatial extent of edge states [45, 47, 48]. Nevertheless, the presence of nonzero $\mathcal{C}$ guarantees that the quantized conductance $\mathcal{C} \times 2e^2/h$ will survive disorder [47], while no such topological protection exists in the case of G/hBN wires whose two-terminal conductance is nonquantized $\lesssim 2e^2/h$ in the presence of edge disorder (figure 3(b)).

Since the usage of the full DFT Hamiltonian is prohibitively expensive for large number of atoms ($\sim 10^6$ in our LB or Kubo formula calculations), we derive simpler *ab initio* TBHs [49]. A widely used approach for this purpose is to transform the DFT Hamiltonian to a basis of maximally localized Wannier functions in a selected energy window around E_F [50]. We combine Wannier TBH (truncated [49] to third NN hoppings without loss of accuracy in the energy window considered in figure 4) with the Kubo formula in figure 4(b), where we find quantized σ_{xy}^v in the gap. Furthermore, due to longer range hoppings, σ_{xy}^v in figure 4(b) has a surprising resilience to short-range disorder that was not exhibited in figure 4(a) for the simplistic TBH of equation (12). However, the same Wannier TBH applied to G/hBN wires generates much larger group velocity $\partial \varepsilon_{k_x}/\hbar \partial k_x$ of edge state bands near the DP (figure A1(d) in appendix A) than in figure 3(a) due to lack of information about atoms (like H) passivating bonds of edge carbon atoms. Nevertheless, such Wannier TBH could be useful for fully encapsulated G/hBN wires, where edges are not exposed to the environment [1, 26].

Therefore, we derive an alternative *ab initio* TBH that precisely fits (figure A1(c) in appendix A) the bands around the DP in figure 3(a). This requires up to the fifth NN hoppings and on-site energies in equation (12), with adjusted values along the edges (figure A2 in appendix A). The *ab initio* 5NN TBH combined with the multiterminal LB formula leads to $R_{NL} \neq 0$, with a sharp peak (figure 2(a)) near the DP in the case of ballistic G/hBN channel. In addition, we also calculate R_{NL} and ρ_{xx} in the presence of disordered edges, where we remove 50% of edge tight-binding sites and also use an additional on-site energy on the remaining edge sites, which is distributed randomly in the range ± 1 eV in order to model binding of different chemical species to the outermost carbon atoms [43] (see figure C1(b) in appendix C for illustration), or bulk of different range (in the model delineated in appendix D). The disorder reduces the height of the R_{NL} peak (figure 2(a)), while concurrently generating a peak in ρ_{xx} (figure 2(b)). Although metallic-like ρ_{xx} in figure 2(b) could arise due to trivial reasons, such as charge inhomogeneity induced by chemical or electrostatic doping at the edges [27], recent imaging [26] of proximity-induced supercurrents flowing near the edges of G/hBN wires is in accord with LDOS in figures 3(c)–(f) or local current distributions in figure C1 in appendix C.

It has been argued [1, 4, 5] that experimental confirmation of topological valley currents carried by the Fermi sea states just beneath the bulk gap E_g is achieved by observing different dependences encoded in equation (1), such as $R_{NL} \propto \rho_{xx}^3$ and $R_{NL} \propto e^{-L/\ell_v}$. However, such dependences were originally derived [16] for the diffusive spin Hall current as the mediative current between the two crossbars, and they can be observed for different types of mediative currents as long as they propagate by diffusion (as demonstrated by the measurements of nonlocal resistance in multiterminal graphene due to direct and inverse spin Hall effect [11]). This is exemplified by figure 5(a) where we find that our mediative edge currents can display $R_{NL} \propto \rho_{xx}^3$ dependence in the presence of experimentally relevant long-range disorder, as well as by figure 5(b) where R_{NL} decays exponentially with increasing channel length L in the presence of strong edge disorder (illustrated in figure C1(b) in appendix C).

Interestingly, the very recent experiments [25] on quasiballistic hBN/G/hBN heterostructures exhibiting metallic-like ρ_{xx} have measured R_{NL} that *does not* scale as $\propto \rho_{xx}^3$ at low temperatures $T \simeq 1.5$ K (such cubic scaling is restored at $T \simeq 40$ K). Also, deep into the insulating regime (i.e., with large ρ_{xx}) R_{NL} becomes independent of ρ_{xx} [5].

Thus, confirming *unambiguously* that R_{NL} originates [1, 4, 5] from topological valley currents carried by the Fermi sea states just beneath the bulk gap E_g requires to demonstrate the scaling $R_{NL} \propto (\sigma_{xy}^v)^2$ in the same regime where $R_{NL} \propto \rho_{xx}^3$ and $R_{NL} \propto e^{-L/\ell_v}$ is found [5]. This, however, is impossible experimentally since σ_{xy}^v is not directly measurable. Nevertheless, $R_{NL}(E_F)$ and $\sigma_{xy}^v(E_F)$ can be calculated independently in a chosen interval of Fermi energies E_F, while using the same long-range or short-range disorder in both the LB and Kubo formula calculations. Figure 2(d) plots $R_{NL}(E_F)$ from figure 2(a) computed using the multiterminal LB formula versus $\sigma_{xy}^v(E_F)$ from figure 4(b) computed using the Kubo formula. In both of these calculations, we employ the *ab initio* 5NN TBH delineated in appendix A in order to avoid $R_{NL} \equiv 0$ in figure 2(c) obtained for the case of the simplistic NN TBH in equation (12).

In conclusion, the R_{NL} peak exists in the clean limit (where $\rho_{xx} \to 0$) and it is reduced by disorder, whereas σ_{xy}^v is insensitive to disorder at the DP (figure 4(b)). Furthermore, plotting $R_{NL}(E_F)$ versus $\sigma_{xy}^v(E_F)$ in figure 2(d), computed for a range of $E_F \geqslant 0$ independently while using the same long-range or short-range disorder in both the LB and Kubo formula calculations, reveals that these two quantities are not related in the way conjectured by equation (1). This strengthens our *principal conclusion*—the observed R_{NL} is driven by a particular gapless band structure and its edge eigenstates carrying current near the DP while not being protected by any nontrivial topology of bulk band structure [66], rather than by the Fermi sea dissipationless topological valley currents conjectured [1–5, 32] for the gapped Dirac spectra.

Acknowledgments

Appendix A. *Ab initio* versus tight-binding band structure of G/hBN wires with zigzag edges

The diagonalization of the KS Hamiltonian in DFT to obtain the *ab initio* band structure proceeds by approximating the Hilbert space of all single-electron eigenfunctions with a finite set of basis functions. A popular basis set is composed of plane-waves (PWs), where varying the energy cutoff makes it possible to improve the basis systematically. Linear combination of atomic orbitals (LCAO) basis sets [51, 41] require more tuning. However, they make it possible to treat supercells containing a large number of atoms with $O(N)$ computational complexity [52, 53]. They also simplify *ab initio* quantum transport device simulations—based on the LB formula combined with the KS Hamiltonian [42]—where one has to spatially separate the devices into a central region and semi-infinite leads (as illustrated by figure 1).

A commonly used minimal LCAO basis set for graphene systems is composed of single-zeta polarized (SZP) pseudoatomic orbitals [51] on C atoms [54]. However, when this is applied to G/hBN wires—together with double-zeta polarized (DZP) orbitals [51] on B and N atoms, and SZP orbitals on edge passivating H atoms—it leads to the valence band of hBN being pushed toward the Fermi level E_F, which incorrectly generates conduction through the hBN substrate. Therefore, we first perform DFT calculations for G/hBN wires with zigzag edges of width $W = 13$ nm using a large LCAO basis set provided in the `OpenMX` package [41] consisting of `s2p1` orbitals on H atoms and `s2p2d1` on C, B and N atoms with cutoff radius 5.0 and 7.0 a.u, respectively. This gives an accurate reference band structure shown in figure A1(a). The same is reproduced by a medium SG15 basis set [55] implemented in the `ATK` package [40], as shown in figure A1(b). For both calculations in figures A1(a) and (b) we use the Perdew–Burke–Ernzerhof (PBE) parametrization of the generalized gradient approximation (GGA) for the exchange-correlation (XC) functional and norm-conserving pseudopotentials for describing electron–core interactions.
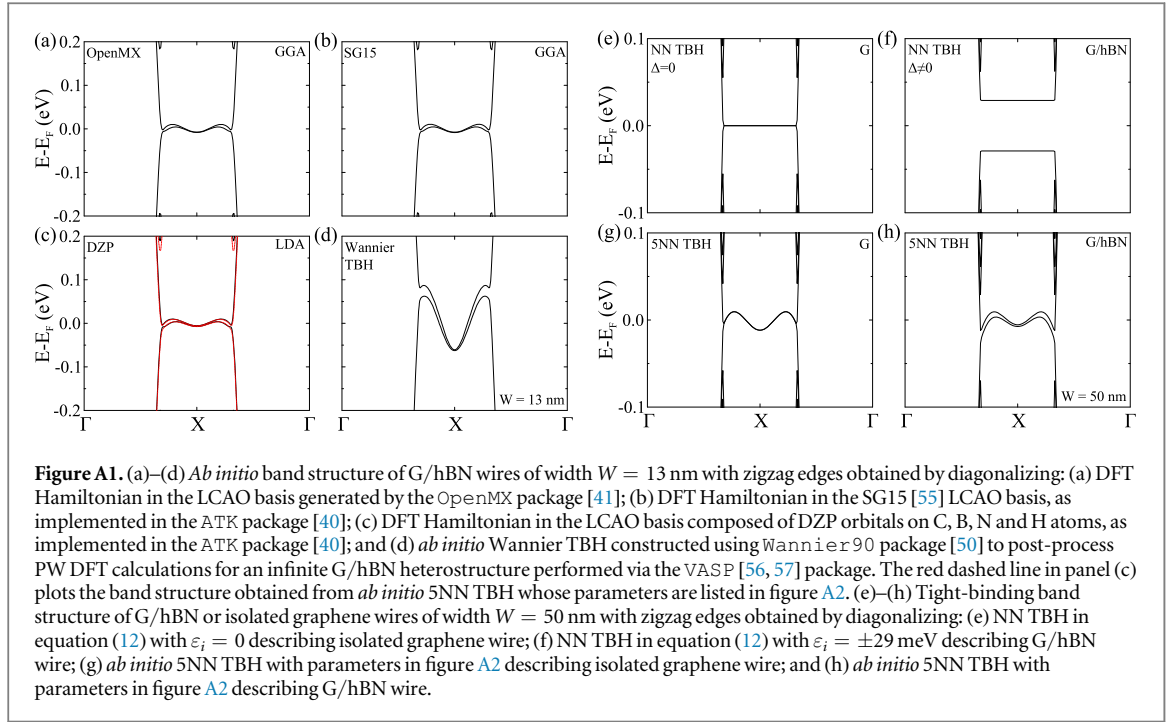
Figure A1. (a)–(d) *Ab initio* band structure of G/hBN wires of width $W = 13$ nm with zigzag edges obtained by diagonalizing: (a) DFT Hamiltonian in the LCAO basis generated by the `OpenMX` package [41]; (b) DFT Hamiltonian in the SG15 [55] LCAO basis, as implemented in the `ATK` package [40]; (c) DFT Hamiltonian in the LCAO basis composed of DZP orbitals on C, B, N and H atoms, as implemented in the `ATK` package [40]; and (d) *ab initio* Wannier TBH constructed using `Wannier90` package [50] to post-process PW DFT calculations for an infinite G/hBN heterostructure performed via the `VASP` [56, 57] package. The red dashed line in panel (c) plots the band structure obtained from *ab initio* 5NN TBH whose parameters are listed in figure A2. (e)–(h) Tight-binding band structure of G/hBN or isolated graphene wires of width $W = 50$ nm with zigzag edges obtained by diagonalizing: (e) NN TBH in equation (12) with $\varepsilon_i = 0$ describing isolated graphene wire; (f) NN TBH in equation (12) with $\varepsilon_i = \pm 29$ meV describing G/hBN wire; (g) *ab initio* 5NN TBH with parameters in figure A2 describing isolated graphene wire; and (h) *ab initio* 5NN TBH with parameters in figure A2 describing G/hBN wire.
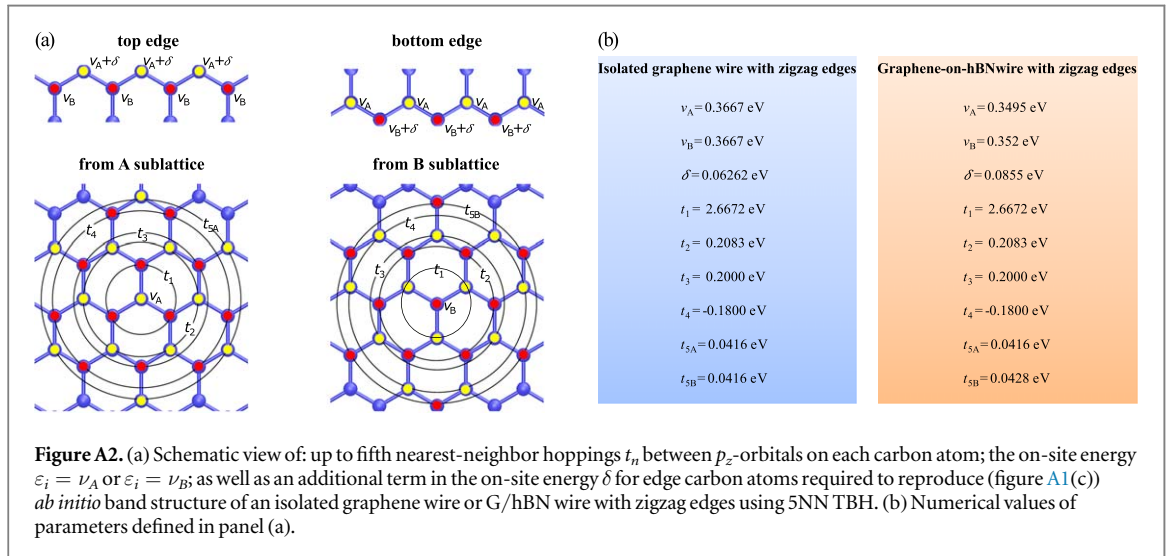
Figure A2. (a) Schematic view of: up to fifth nearest-neighbor hoppings t_n between p_z-orbitals on each carbon atom; the on-site energy $\varepsilon_i = \nu_A$ or $\varepsilon_i = \nu_B$; as well as an additional term in the on-site energy δ for edge carbon atoms required to reproduce (figure A1(c)) *ab initio* band structure of an isolated graphene wire or G/hBN wire with zigzag edges using 5NN TBH. (b) Numerical values of parameters defined in panel (a).

However, the matrix representations of the KS Hamiltonian in both the `OpenMX` and in the smaller SG15 basis sets are still too large for computationally efficient quantum transport simulations. Therefore, we perform additional calculations using DZP orbitals on all atoms C, B, N, and H and Perdew–Zunger parametrization of the local density approximation (LDA) for the XC functional, which produces a reasonably small KS Hamiltonian matrix. The corresponding band structure in figure A1(c) matches the band structure obtained in figures A1(a) and (b) in the energy interval ± 0.1 eV around the DP at $E - E_F = 0$, which is of interest to quantum transport studies in the linear-response regime. The same match (not shown explicitly) remains valid for G/hBN wires of width $W = 50$ nm employed as the channel of the device in figure 1. The matrix representation of the KS Hamiltonian in the basis of DZP orbitals is employed to obtain LDOS and conductance of two-terminal wires in figures 3 and B1.

The very large number of atoms $\sim 10^6$ in our Kubo or multiterminal LB formula calculations makes the direct usage of KS Hamiltonian prohibitively expensive [42]. Instead, a Hamiltonian with a minimal number of orbitals *per* atom, as provided by semi-empirical or *ab initio* TBHs, is required. A widely used approach to derive an accurate *ab initio* TBH [49] is to project the KS Hamiltonian onto a basis of maximally localized Wannier functions, which faithfully retains the overlap matrix elements and their phases, the orbital character of the bands and the accuracy of the original DFT calculations [50]. We compute the KS Hamiltonian in the PW basis

using the VASP package [56, 57], where we consider p_x, p_y and p_z orbitals on C atoms for bands around the DP of an infinite G/hBN heterostructure. In the VASP calculations, we choose a PW cutoff energy 500 eV, the PBE parametrization of the GGA for the XC functional, and the projector augmented wave method for describing electron–core interactions [58, 59]. The k-point mesh of size $8 \times 6 \times 1$ is used for the Brillouin zone (BZ) sampling of a rectangular unit cell consisting of four C atoms.

Thus, the derived Wannier TBH, truncated [49] to third NN hoppings without loss of accuracy of band structure in the interval considered in figure 4(b), is useful for the Kubo formula calculations (figure 4(b)) on rhomboid supercells with periodic boundary conditions. However, the Wannier TBH generates a too large group velocity $\partial \varepsilon_{k_x} / \hbar \partial k_x$ of edge state bands near the DP in figure A1(d) when compared to those in figures A1(a)–(c) obtained directly from DFT calculations. This is because the VASP calculations for the periodic supercell of G/hBN used to construct the Wannier TBH did not include information about edges and edge passivating atoms. Nevertheless, the Wannier TBH could be useful for fully encapsulated hBN/G/hBN wires [25, 26], where edges are not exposed to the environment and where a large group velocity of edge state bands near the DP in figure A1(d) would make edge currents *more resilient* to disorder.

Therefore, we resort to the construction of another *ab initio* TBH via the least square fitting [60] of the bands around the DP, as shown in figure A1(c), while keeping in mind possible problems with overfitting [49]. Such *ab initio* TBH with single p_z-orbital *per* site includes up to fifth NN hoppings and on-site energies illustrated in figure A2(a) and listed in figure A2(b). The *ab initio* 5NN TBH is used in the computation of R_{NL} in figures 2(a), 2(d), 5 and B2; ρ_{xx} in figure 2(b); and local current distribution in figure C1.
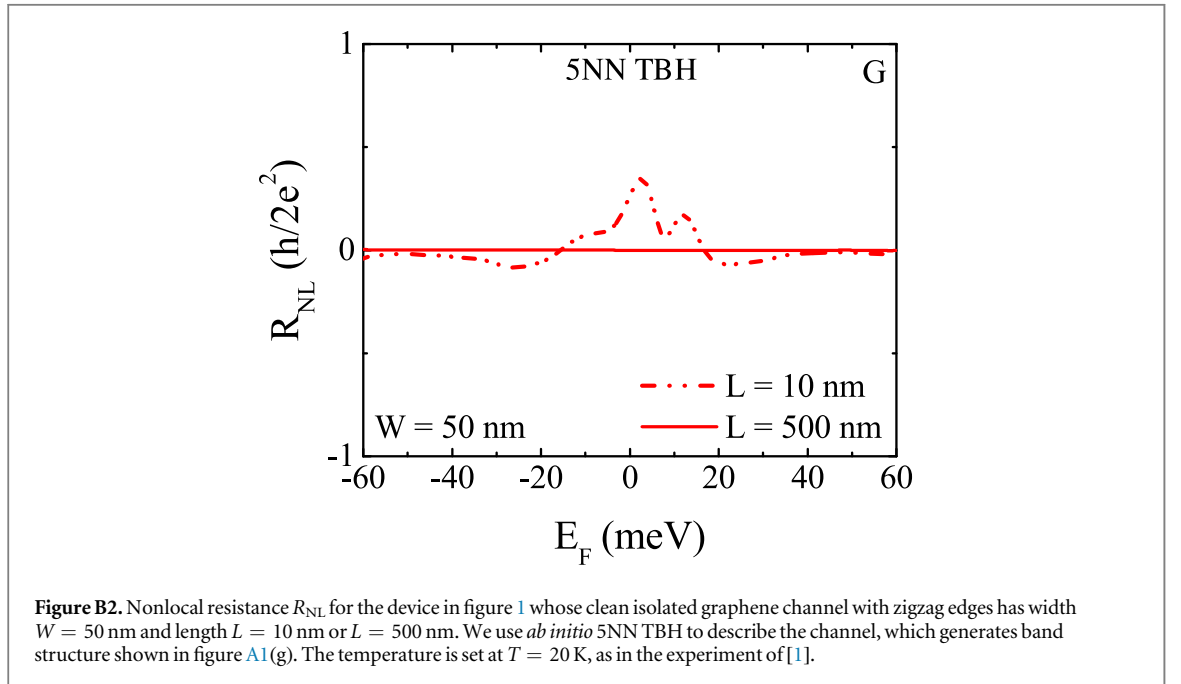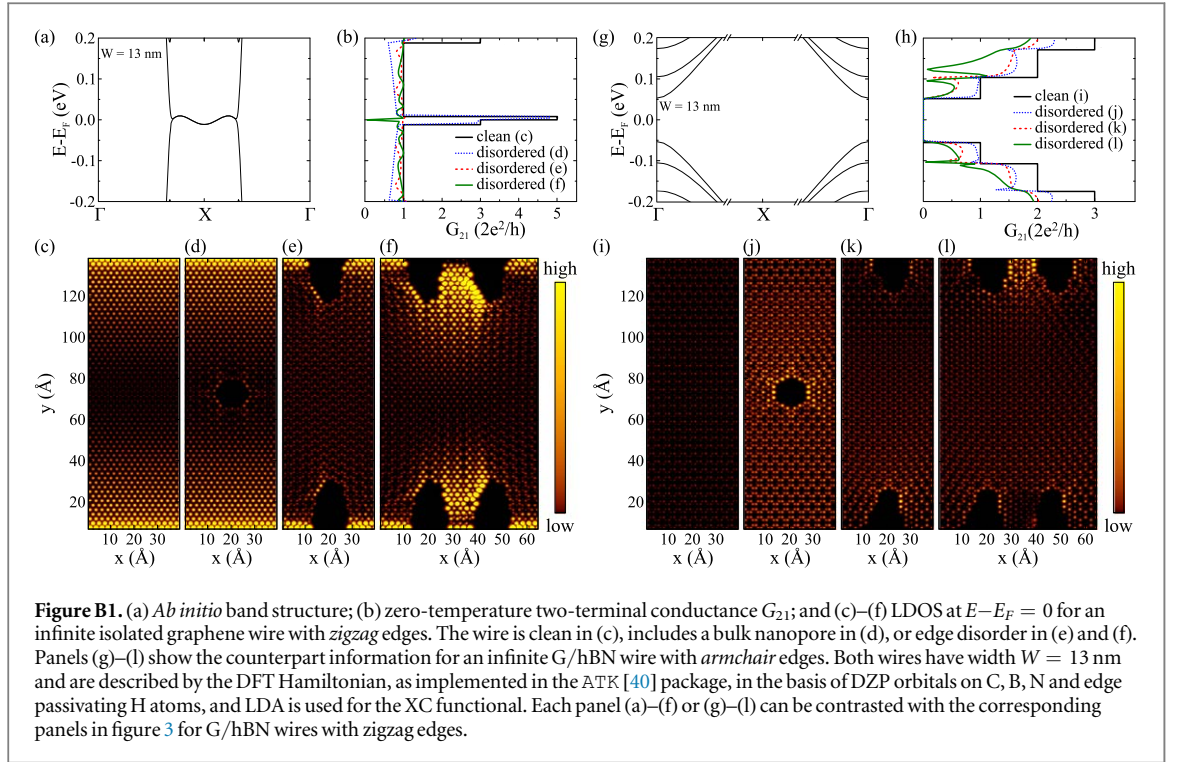
Figures A1(e) and (f) plot the band structure of isolated graphene and G/hBN wires, both with zigzag edges and width $W = 50$ nm, respectively, obtained by diagonalizing the simplistic TBH in equation (12), which includes only the NN hopping [32]. The same band structures are recomputed in figures A1(g) and (h), respectively, using the *ab initio* 5NN TBH from figure A2. The nonlocal resistances R_{NL} for channels of multiterminal device in figure 1 with band structures shown in figures A1(h), (f) and (g) are plotted in figures 2(a), (c) and B2, respectively. The gapped band structure in figure A1(f) for the simplistic NN TBH in equation (12) was obtained previously in [32]. The flat bands connecting the two valleys at the gap boundary correspond to edge states, and they are inherited from the band structure of an isolated graphene wire with zigzag edges shown in figure A1(e). That is, simulating the presence of hBN by using the staggered on-site energy $\varepsilon_i = \pm \Delta$ in NN TBN in equation (12) simply opens the gap between the flat bands in figure A1(e) to produce the band structure in figure A1(f). Both of these band structures, which are an artifact of the simplistic NN TBH [31, 61] or continuous Dirac Hamiltonian with appropriate boundary conditions [62], *do not* generate edge currents [63]. This *contradicts* experimental observation of edge currents near the DP in isolated graphene wires with zigzag edges [28] or in G/hBN wires where some zigzag segments are present [26]. These edge currents [26] are responsible for the metallic-like resistivity ρ_{xx} in figure 2(b), which is also observed experimentally [1, 25, 26].

Appendix B. *Ab initio* band structure and quantum transport through isolated graphene wire with zigzag edges or G/hBN wire with armchair edges

For comparison with figure 3, we provide identically calculated panels in figures B1(a)–(f) for an isolated graphene wire with zigzag edges and in figures B1(g)–(l) for a G/hBN wire with armchair edges, both of the same width $W = 13$ nm. For this purpose, we use LCAO pseudopotential DFT implemented in the ATK package [40], where the KS Hamiltonian is represented in the basis of DZP orbitals on C, B, N and H atoms, LDA is used for XC functional and the energy mesh cutoff for the real-space grid is chosen as 75.0 Hartree. Careful comparison shows that the hBN substrate splits the edge bands near the DP—see inset in figure 3(a)—and also slightly changes the spatial extension of the corresponding eigenstates. This helps to make conductance in figure 3(b) more resilient to quantum interference effects in the case of a series of edge vacancies in figure 3(f), thereby evading antiresonance in the conductance at the DP in figure B1(b).

Despite the existence of edge eigenstates in isolated graphene wires with zigzag edges, using its *ab initio* 5NN TBH to describe the channel of the device in figure 1 leads to $R_{\mathrm{NL}} \equiv 0$ in figure B2 for $L \gg W$ geometry. This is in accord with experiments of [1] or figure 2(a), where aligned hBN is *necessary* to obtain $R_{\mathrm{NL}} \neq 0$ by modifying the energy–momentum dispersion of edge eigenstates from that shown in figure A1(g) to the one shown in figure A1(h).

In contrast to the simplistic NN TBH for an isolated graphene wire with armchair edges, which predicts that those composed of $3p + 2$ dimers are metallic [61], DFT calculations show that armchair wires of all widths have an energy gap [61]. The energy gap in figure B1(g) of G/hBN wires with armchair edges can be larger (depending on the wire width) than the gap $E_g \simeq 58$ meV [13] of bulk G/hBN because of transverse confinement in the case of wire geometry. As shown in figures B1(i)–(l), such gapped wires have no edge states around the DP. Since their two-terminal conductance G_{21} in figure B1(h) is zero within the gap, using G/hBN wires with

Figure B1. (a) *Ab initio* band structure; (b) zero-temperature two-terminal conductance G_{21}; and (c)–(f) LDOS at $E-E_F = 0$ for an infinite isolated graphene wire with *zigzag* edges. The wire is clean in (c), includes a bulk nanopore in (d), or edge disorder in (e) and (f). Panels (g)–(l) show the counterpart information for an infinite G/hBN wire with *armchair* edges. Both wires have width $W = 13$ nm and are described by the DFT Hamiltonian, as implemented in the ATK [40] package, in the basis of DZP orbitals on C, B, N and edge passivating H atoms, and LDA is used for the XC functional. Each panel (a)–(f) or (g)–(l) can be contrasted with the corresponding panels in figure 3 for G/hBN wires with zigzag edges.

Figure B2. Nonlocal resistance R_{NL} for the device in figure 1 whose clean isolated graphene channel with zigzag edges has width $W = 50$ nm and length $L = 10$ nm or $L = 500$ nm. We use *ab initio* 5NN TBH to describe the channel, which generates band structure shown in figure A1(g). The temperature is set at $T = 20$ K, as in the experiment of [1].

armchair edges as the channel between the two crossbars in the device in figure 1 leads to $R_{NL} \equiv 0$ for $L \gg W$ geometry.

Appendix C. Local current distribution in clean or edge-disordered G/hBN wires with zigzag edges

Figure C1 plots the local current distribution in G/hBN wires with zigzag edges, where current at a site of the tight-binding lattice is obtained by summing all bond currents [63, 64] flowing from that site to all other sites to which it is connected by nonzero hoppings of the *ab initio* 5NN TBH in figure A2. In the case of an infinite clean homogeneous G/hBN wire with zigzag edges, figure C1(a) reveals edge currents flowing in narrow strips near the edge with minuscule value flowing through the bulk [31]. Upon introducing edge disorder [43], whose

Figure C1. Local current distribution in an infinite G/hBN wire with zigzag edges of width $W = 13$ nm described by the *ab initio* 5NN TBH in figure A2, which generates band structure shown in figure A1(h). The wire is clean homogeneous in (a) or edge-disordered in (c). The edge disorder, introduced on both edges over the length of 20 nm, is illustrated in panel (b) where we remove 50% of edge tight-binding sites and also use an additional on-site energy on the remaining edge sites, which is distributed randomly in the range ± 1 eV in order to model binding of different chemical species to the outermost carbon atoms [43].

properties are defined in figure C1(b) and which is also used to compute edge disorder effects on R_{NL} and ρ_{xx} in figures 2 and 5(b), we find that some part of the electron flux is deflected into the bulk of the wire. Nevertheless, as long as the G/hBN wire contains short zigzag-edge segments local current is confined near the edges, in agreement with very recent experimental imaging [26] of proximity-induced supercurrents in G/hBN wires.

Appendix D. Models for long-range and short-range disorder in the bulk

The long-range and short-range disorder—employed in the LB formula calculations in figures 2 and 5(a), as well as in the Kubo formula calculations in figure 4—is modeled as additional on-site energy terms in TBHs

$$\hat{V} = \sum_{n=1}^{N_p} V_i(\mathbf{R}_n) \hat{c}_i^\dagger \hat{c}_i, \tag{D.1}$$

where N_p is the number of impurities, $\hat{c}_i^\dagger$ ($\hat{c}_i$) creates (annihilates) an electron at site i and

$$V_i(\mathbf{R}_n) = \frac{U_n}{\sum_{i=1}^{N_{\mathrm{tot}}} e^{-(\mathbf{r}_i - \mathbf{R}_n)^2/2\xi^2}} e^{-(\mathbf{r}_i - \mathbf{R}_n)^2/2\xi^2}, \tag{D.2}$$

is the contribution at site i due to an impurity placed at position $\mathbf{R}_n$. Here N_{tot} is the total number of lattice sites, U_n is a uniform random variable in the interval $[-U_p, U_p]$ and ξ is the spatial range of the impurity potential.

Using this definition, the parameter K_0 in the Gaussian correlator ($\langle\ldots\rangle$ denotes disorder averaging)

$$\sum_{n,m}\langle V_i(\mathbf{R}_m)\,V_j(\mathbf{R}_n)\rangle = K_0\frac{(\hbar v_F)^2}{2\pi\xi^2}e^{-(\mathbf{r}_i-\mathbf{r}_j)^2/2\xi^2},\tag{D.3}$$

is given by $K_0\sim N_p\,N_{\text{tot}}\,U_p^4/t_1^4$ (t_1 is NN hopping) and it is independent of the spatial range ξ. This definition is similar to the one used in previous studies [17, 18, 65], but it employs a range-dependent strength of the impurity potential, which allows us to compare impurity potentials with the same U_p but different ξ parameters. The short-range disorder employed in figures 2, 4 and 5(a) is modeled using $\xi = 0.1a_{C-C}$ and strength $U_p = 1.275$ eV, while for long-range disorder we use $\xi = 10a_{C-C}$ and effective strength $\simeq 0.005\times U_p$, where $a_{C-C}\approx 1.42$ Å is the carbon–carbon bond length. Thus, such long-range disorder can capture puddles induced by charged impurities of effective strength ~ 10 meV, which is similar to realistic samples where the depth of the charged puddles is of the same order as the gap E_g.

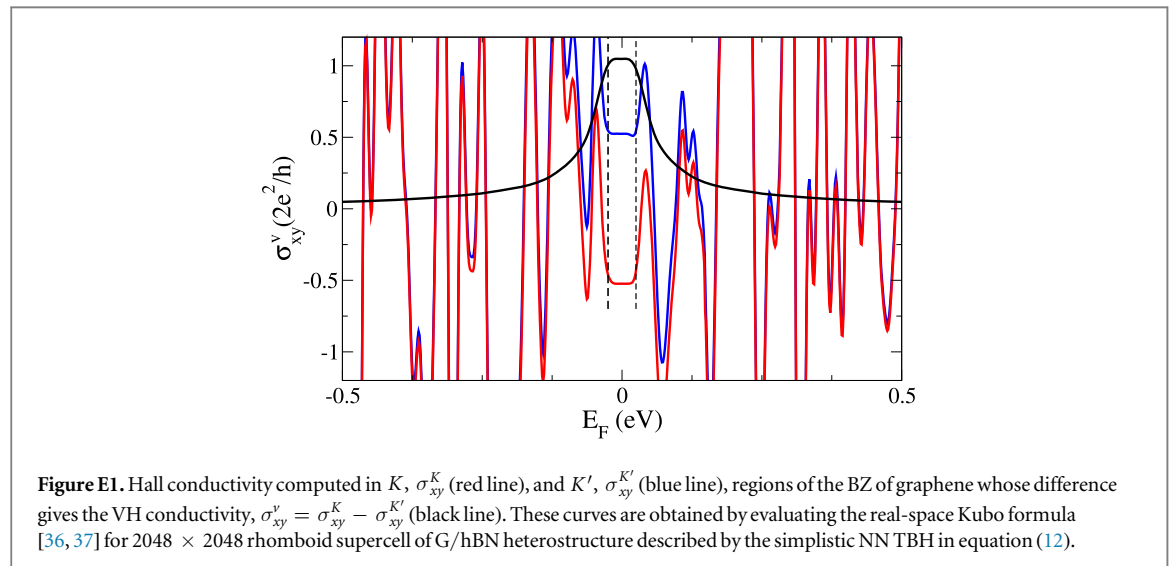## Appendix E. Valley-projection scheme for Kubo formula calculations

The valley-projection scheme [10, 39] we employ for numerically exact calculations of the VH conductivity σ_{xy}^v in figure 4 via the real-space Kubo formula [36, 37] relies on the artificial separation of the BZ of graphene into K and K' regions with different chirality. In this scheme, the current defined over the whole BZ is separated into an electronic current due electrons in the $K(K')$ valley. This can be done by projecting the α-component of the velocity operator in the following way

$$\hat{v}_\alpha^{\vec{K}(\vec{K}')}\equiv P_{\vec{K}(\vec{K}')}\hat{v}_\alpha P_{\vec{K}(\vec{K}')},\tag{E.1}$$

where

$$P_{\vec{K}(\vec{K}')}=\sum_{\vec{q}}w_{\vec{q}}^{\vec{K}(\vec{K}')}|q\rangle\langle q|,\tag{E.2}$$

with the sum going over the whole BZ. The weight, $w_{\vec{q}}^{\vec{K}}=\Theta[(\vec{q}-\vec{M})\cdot(\vec{K}-\vec{M})/|\vec{K}-\vec{M}|^2]$, breaks the BZ into two regions, one containing the $\vec{K}$ point, which has unit weight, and another which contains the $\vec{K}'$ point with zero weight. The weight $w_{\vec{q}}^{\vec{K}'}$ is defined as $w_{\vec{q}}^{\vec{K}'}\equiv 1-w_{\vec{q}}^{\vec{K}}$. As shown in figure E1, when computing the Hall conductivities for each of the two valleys, σ_{xy}^K and $\sigma_{xy}^{K'}$, a lot of noise is generated from stochastic calculation of the trace in the real-space Kubo formula [36, 37]. These fluctuations are random and as such do not obey any symmetry of the system. But once we compute the VH conductivity, $\sigma_{xy}^v=\sigma_{xy}^K-\sigma_{xy}^{K'}$, this noise is filtered away because it does not have opposite chirality. However, when we introduce disorder effects that scatter electrons between the two valleys, such a property is removed and one should proceed to smooth out these fluctuations by averaging over many disorder realizations.

Figure E1. Hall conductivity computed in K, σ_{xy}^K (red line), and K', $\sigma_{xy}^{K'}$ (blue line), regions of the BZ of graphene whose difference gives the VH conductivity, $\sigma_{xy}^v=\sigma_{xy}^K-\sigma_{xy}^{K'}$ (black line). These curves are obtained by evaluating the real-space Kubo formula [36, 37] for 2048 × 2048 rhomboid supercell of G/hBN heterostructure described by the simplistic NN TBH in equation (12).

ORCID iDs

J M Marmolejo-Tejada ⬤ https://orcid.org/0000-0002-2363-5100
J H García ⬤ https://orcid.org/0000-0002-5752-4759
A Cresti ⬤ https://orcid.org/0000-0002-1326-2515
S Roche ⬤ https://orcid.org/0000-0003-0323-4665
B K Nikolić ⬤ https://orcid.org/0000-0002-5793-7764

References

[1] Gorbachev R V *et al* 2014 *Science* **346** 448
[2] Xiao D, Yao W and Niu Q 2007 *Phys. Rev. Lett.* **99** 236809
[3] Lensky Y D, Song J C W, Samutpraphoot P and Levitov L S 2015 *Phys. Rev. Lett.* **114** 256601
[4] Song J C W, Samutpraphoot P and Levitov L S 2015 *Proc. Natl Acad. Soc.* **112** 10879
[5] Beconcini M, Taddei F and Polini M 2016 *Phys. Rev. B* **94** 121408
[6] Abanin D A *et al* 2011 *Science* **332** 328
[7] Renard J, Studer M and Folk J A 2014 *Phys. Rev. Lett.* **112** 116601
[8] Wei P *et al* 2016 *Nat. Mater.* **15** 711
[9] Chen C-L, Chang C-R and Nikolić B K 2012 *Phys. Rev. B* **85** 155414
[10] Cresti A, Nikolić B K, García J H and Roche S 2016 *Riv. Nuovo Cimento* **39** 587
[11] Balakrishnan J, Balakrishnan J, Koon G K W, Jaiswal M, Castro Neto A H and Özyilmaz B 2013 *Nat. Phys.* **9** 284
    Balakrishnan J *et al* 2014 *Nat. Commun.* **5** 4748
    Avsar A *et al* 2014 *Nat. Commun.* **5** 4875
[12] Van Tuan D, Marmolejo-Tejada J M, Waintal X, Nikolić B K, Valenzuela S O and Roche S 2016 *Phys. Rev. Lett.* **117** 176602
[13] Giovannetti G, Khomyakov P A, Brocks G, Kelly P J and van den Brink J 2007 *Phys. Rev. B* **76** 073103
[14] Xiao D, Chang M-C and Niu Q 2010 *Rev. Mod. Phys.* **82** 1959
    Nagaosa N, Sinova J, Onoda S, MacDonald A H and Ong N P 2010 *Rev. Mod. Phys.* **82** 1539
[15] Ando T 2015 *J. Phys. Soc. Japan* **84** 114705
[16] Abanin D A, Shytov A V, Levitov L S and Halperin B I 2009 *Phys. Rev. B* **79** 035304
[17] Adam S, Brouwer P W and Das Sarma S 2009 *Phys. Rev. B* **79** 201404
[18] Kłos J W and Zozoulenko I V 2010 *Phys. Rev. B* **82** 081414
[19] Kirczenow G 2015 *Phys. Rev. B* **92** 125425
[20] Büttiker M 1986 *Phys. Rev. Lett.* **57** 1761
[21] Baranger H U and Stone A D 1989 *Phys. Rev. B* **40** 8169
[22] Groth C W, Wimmer M, Akhmerov A R and Waintal X 2014 *New J. Phys.* **16** 063065
[23] McEuen P L, Szafer A, Richter C A, Alphenaar B W, Jain J K, Stone A D, Wheeler R G and Sacks R N 1990 *Phys. Rev. Lett.* **64** 2062
[24] Roth A, Brüne C, Buhmann H, Molenkamp L W, Maciejko J, Qi X-L and Zhang S-C 2009 *Science* **325** 294
[25] Komatsu K, Morita Y, Watanabe E, Tsuya D, Watanabe K, Taniguchi T and Moriyama S 2018 *Sci. Adv.* **4** eaaq0194
[26] Zhu M J *et al* 2017 *Nat. Commun.* **8** 14552
[27] Dou Z *et al* 2018 *Nano Lett.* **18** 2530
[28] Jia X *et al* 2009 *Science* **323** 1701
[29] Saha K K, Drndić M and Nikolić B K 2012 *Nano Lett.* **12** 50
    Chang P-H, Liu H and Nikolić B K 2014 *J. Comput. Electron.* **13** 847
[30] Tao C *et al* 2011 *Nat. Phys.* **7** 616
[31] Chang P-H and Nikolić B K 2012 *Phys. Rev. B* **86** 041406(R)
[32] Yao W, Yang S A and Niu Q 2009 *Phys. Rev. Lett.* **102** 096801
    Ren Y, Qiao Z and Niu Q 2016 *Rep. Prog. Phys.* **79** 066501
[33] Puetter C M, Konabe S, Tokura Y, Hatsugai Y and Shiraishi K 2012 (arXiv:1211.0150)
[34] Groth C W, Wimmer M, Akhmerov A R and Waintal X 2014 *New J. Phys.* **16** 063065
[35] Bastin A, Lewinner C, Betbeder-Matibet O and Nozieres P 1971 *J. Phys. Chem. Solids* **32** 1811
[36] Ferreira A and Mucciolo E R 2015 *Phys. Rev. Lett.* **115** 106601
[37] García J H, Covaci L and Rappoport T G 2015 *Phys. Rev. Lett.* **114** 116602
    García J H and Rappoport T G 2016 *2D Mater.* **3** 024007
[38] Nikolić B K, Zârbo L P and Welack S 2005 *Phys. Rev. B* **72** 075335
[39] Settnes M, García J H and Roche S 2017 *2D Mater.* **4** 031006
[40] Atomistix Toolkit version 2016.4, Synopsys QuantumWise A/S http://quantumwise.com
[41] Ozaki T 2003 *Phys. Rev. B* **67** 155108
    Ozaki T and Kino H 2004 *Phys. Rev. B* **69** 195113
    Ozaki T and Kino H 2005 *Phys. Rev. B* **72** 045121
    Lejaeghere K *et al* 2016 *Science* **351** aad3000
[42] Brandbyge M, Mozos J-L, Ordejón P, Taylor J and Stokbro K 2002 *Phys. Rev. B* **65** 165401
    Areshkin D A and Nikolić B K 2010 *Phys. Rev. B* **81** 155450
    Sanvito S 2011 Electron transport theory for large systems *Comput. Nanosci.* ed E Bichoutskaia (Cambridge: RSC Publishing)
    Papior N, Lorente N, Frederiksen T, García A and Brandbyge M 2017 *Comput. Phys. Commun.* **212** 8
[43] Li J, Martin I, Büttiker M and Morpurgo A F 2011 *Nat. Phys.* **7** 38
[44] Rycerz A, Tworzydło J and Beenakker C W J 2007 *Nat. Phys.* **3** 172
[45] Chang P-H, Bahramy M S, Nagaosa N and Nikolić B K 2014 *Nano Lett.* **14** 3779
[46] Cresti A, Van Tuan D, Soriano D, Cummings A W and Roche S 2014 *Phys. Rev. Lett.* **113** 246603
[47] Sheng X-L and Nikolić B K 2017 *Phys. Rev. B* **95** 201402(R)
[48] Prada E and Metalidis G 2013 *J. Comput. Electron.* **12** 63
[49] Fang S, Defo R K, Shirodkar S N, Lieu S, Tritsaris G A and Kaxiras E 2015 *Phys. Rev. B* **92** 205108

[50] Marzari N, Mostofi A A, Yates J R, Souza I and Vanderbilt D 2012 *Rev. Mod. Phys.* **84** 1419

Mostofi A A, Yates J R, Lee Y-S, Souza I, Vanderbilt D and Marzari N 2008 *Comput. Phys. Commun.* **178** 685

[51] Junquera J, Paz O, Sánchez-Portal D and Artacho E 2001 *Phys. Rev. B* **64** 235111

[52] Ozaki T 2006 *Phys. Rev. B* **74** 245101

[53] Bowler D R and Miyazaki T 2012 *Rep. Prog. Phys.* **75** 036503

[54] Agapito L A, Fornari M, Ceresoli D, Ferretti A, Curtarolo S and Nardelli M B 2016 *Phys. Rev. B* **93** 125137

[55] Schlipf M and Gygi F 2015 *Comput. Phys. Commun.* **196** 36

[56] Kresse G and Hafner J 1993 *Phys. Rev. B* **47** 558

[57] Kresse G and Furthmüller J 1996 *Comput. Mater. Sci.* **6** 15

[58] Blöchl P E 1994 *Phys. Rev. B* **50** 17953

[59] Kresse G and Joubert D 1999 *Phys. Rev. B* **59** 1758

[60] Ridolfi E, Le D, Rahman T S, Mucciolo E R and Lewenkopf C H 2015 *J. Phys.: Condens. Matter* **27** 365501

[61] Boykin T B, Luisier M, Klimeck G, Jiang X, Kharche N, Zhou Y and Nayak S K 2011 *J. Appl. Phys.* **109** 104304

[62] Brey L and Fertig H A 2006 *Phys. Rev. B* **73** 235411

Winkler R and Deshpande H 2017 *Phys. Rev. B* **95** 235312

[63] Zârbo L P and Nikolić B K 2007 *Europhys. Lett.* **80** 47001

[64] Cresti A, Farchioni R, Grosso G and Parravicini G P 2003 *Phys. Rev. B* **68** 075306

[65] Ortmann F, Cresti A, Montambaux G and Roche S 2011 *Europhys. Lett.* **94** 47006

[66] Haldane F D M 2017 *Rev. Mod. Phys.* **89** 040502